Prolonged Orbital Relaxation by Locally Modified Phonon Density of States for the SiV^- Center in Nanodiamonds

M. Klotz,[1,*] K. G. Fehler,[1,*] R. Waltrich,[1] E. S. Steiger,[1] S. Häußler,[1] P. Reddy,[2] L. F. Kulikova,[3] V. A. Davydov,[3] V. N. Agafonov,[4] M. W. Doherty,[2] and A. Kubanek[1,†]

[1]*Institute for Quantum Optics, Ulm University, 89081 Ulm, Germany*

[2]*Laser Physics Centre, Research School of Physics, Australian National University, Australian Capital Territory 2601, Australia*

[3]*L.F. Vereshchagin Institute for High Pressure Physics, Russian Academy of Sciences, Troitsk, Moscow 142190, Russia*

[4]*GREMAN, UMR 7347 CNRS, INSA-CVL, Tours University, 37200 Tours, France*

(Received 3 August 2021; revised 16 December 2021; accepted 1 February 2022; published 12 April 2022)

Coherent quantum systems are a key resource for emerging quantum technology. Solid-state spin systems are of particular importance for compact and scalable devices. However, interaction with the solid-state host degrades the coherence properties. The negatively charged silicon vacancy center in diamond is such an example. While spectral properties are outstanding, with optical coherence protected by the defects symmetry, the spin coherence is susceptible to rapid orbital relaxation limiting the spin dephasing time. A prolongation of the orbital relaxation time is therefore of utmost urgency and has been tackled by operating at very low temperatures or by introducing large strain. However, both methods have significant drawbacks: the former requires use of dilution refrigerators and the latter affects intrinsic symmetries. Here, a novel method is presented to prolong the orbital relaxation with a locally modified phonon density of states in the relevant frequency range, by restricting the diamond host to below 100 nm. Subsequently measured coherent population trapping shows an extended spin dephasing time compared to the phonon-limited time in a pure bulk diamond. The method works at liquid helium temperatures of few Kelvin and in the low-strain regime.

DOI: 10.1103/PhysRevLett.128.153602

Color centers in diamond, in particular the negatively charged silicon vacancy center in diamond (SiV^-), turned out to be a promising system to realize applications that rely on an efficient spin-photon interface and long-lived memories [1], for example, in the context of quantum communication [2]. However, such sophisticated experiments require us to suppress the host's strong environmental influence on the optical and spin coherence. Here, the group-IV defect centers stand out due to their inversion symmetry which protects their optical transitions against charge fluctuations from, e.g., close-by surfaces, when integrated into nanostructures [3]. As a result, SiV^- exhibit narrow inhomogeneous line distribution and excellent spectral stability [4]. Because of its relatively small orbital extension as compared to other group-IV defects, SiV^- is highly susceptible to strain introduced by electron-phonon interactions with the environment [5]. Ultimately this limits the spin coherence time (T_2) due to a short dephasing time (T_2^*) related to orbital transitions in the ground state (GS) [6]. For temperatures below 25 K, the orbital relaxation rate (Γ_1) is dominated by a single acoustic phonon process, resonant to the ground-state splitting of $\Delta_{\mathrm{GS}}/2\pi \approx 46$ GHz as a result of spin-orbit (SO) interaction [7]. Therefore, even for high-purity, low-strain bulk diamond the orbital relaxation time (T_1) is limited to tens of nanoseconds at liquid helium temperature. Hence, for applications relying on long T_2 it is crucial to decrease Γ_1 such that T_2^* is no longer limited by orbital relaxation but rather by intrinsic, material related noise sources, such as dipolar coupling to the nuclear spin bath or g-factor fluctuations. There are two possibilities to influence Γ_1. First, decreasing temperature T reduces thermal occupation of phonon modes at relevant frequencies Δ_{GS} [1]. Experiments have been performed at $T = 100$ mK yielding $T_2 = 13$ μs, where $k_B T \ll \hbar\Delta_{\mathrm{GS}}$. Already at 2–4 K, $T_2^* \approx 100$ ns is significantly shortened [1,8]. Second, changing the geometry or applying an external load alters the SiV^- strain environment and hence locally modifies the spectral coupling density. Imposing an external force has been done by means of a nanoelectromechanical system, which resulted in prolonged T_2^* of 0.25 μs for a GS splitting of 467 GHz [9]. This work presents a T_1 and T_2^* prolongation of SiV^- incorporated into a geometrically confined host, namely a nanodiamond (ND), in direct thermal contact with a cooled base substrate; see Fig. 1. Accompanying numerical simulations give detailed insights into the defect's strain response.

Model.—The ground-state manifold SiV^- Hamiltonian considered here is given by ($\hbar = 1$)

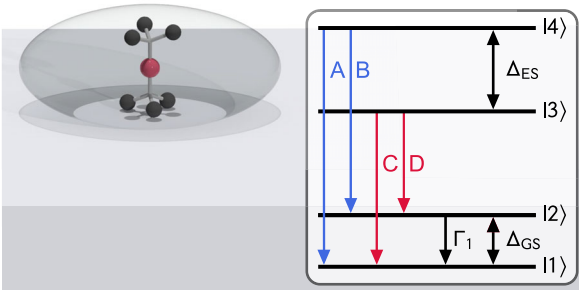

FIG. 1. Schematic of a geometrically confined SiV^- within a ND placed on a diamond substrate. The defect's level structure is also depicted with its zero-phonon-line transitions A, B, C, and D. The GS splitting Δ_{GS} is a result from spin-orbit as well as mechanical interaction with the environment, which leads to an orbital relaxation from $|2\rangle \rightarrow |1\rangle$ with rate Γ_1, where, e.g., $|2\rangle = |e_{g_-}\uparrow\rangle$ and $|1\rangle = |e_{g_+}\uparrow\rangle$ in a strain-free environment.

$$H_{\mathrm{SiV}} = -\frac{\lambda_{\mathrm{SO}}}{2}\sigma_{y,o}\otimes\sigma_{z,s} + \chi_{E_{\mathrm{gx}}}\epsilon_{E_{\mathrm{gx}}}\sigma_{z,o}\otimes\mathbb{1}_s + \chi_{E_{\mathrm{gy}}}\epsilon_{E_{\mathrm{gy}}}\sigma_{x,o}\otimes\mathbb{1}_s, \quad (1)$$

where $\sigma_{i,\mathrm{o}}$ and $\sigma_{i,\mathrm{s}}$ are orbital and spin Pauli operators, $\lambda_{\mathrm{SO}}/2\pi = 46$ GHz the spin-orbit interaction strength, and

$$\chi_{E_{\mathrm{gx}}}\epsilon_{E_{\mathrm{gx}}} = \alpha(\epsilon_{xx} - \epsilon_{yy}) + \beta\epsilon_{zx}, \quad (2)$$

$$\chi_{E_{\mathrm{gy}}}\epsilon_{E_{\mathrm{gy}}} = -2\alpha\epsilon_{xy} + \beta\epsilon_{yz} \quad (3)$$

are symmetry adapted linear combinations of strain field components describing the phononic interaction [10,11]. More details on the derivation of Eq. (1) can be found in the Supplemental Material (SM) [12].

As a consequence of this interaction, the pure spin-orbit eigenstates $|e_{g_+}\uparrow\rangle, |e_{g_-}\downarrow\rangle$ and $|e_{g_+}\downarrow\rangle, |e_{g_-}\uparrow\rangle$ with an energy splitting of $\Delta_{\mathrm{GS}} = \lambda_{\mathrm{SO}}$ will shift in relative energies and also undergo relaxations with rate Γ_1; see Fig. 1. The strain-dependent transition rate from the excited to the ground state is calculated by Fermi's golden rule ($T \rightarrow 0$):

$$\Gamma_1^0 = 2\pi\sum_n (|\chi_{E_{\mathrm{gx}}}\epsilon_{E_{\mathrm{gx}},n}|^2 + |\chi_{E_{\mathrm{gy}}}\epsilon_{E_{\mathrm{gy}},n}|^2)\delta(\omega_n - \Delta_{\mathrm{GS}}). \quad (4)$$

Here n labels the various coupled system eigenfrequencies. Local increase in $T_1^0 = (\Gamma_1^0)^{-1}$ compared to bulk $T_1^{0,B}$ is estimated by utilizing 3D FEM to solve for the mechanical eigenfrequencies of a ND coupled to a diamond substrate. The material properties are assumed to be isotropic with mass density $\rho = 3515$ kg m^{-3}, Young's modulus $E = 1050$ GPa, and Poisson ratio $\nu = 0.2$ [11,16].

Although the NDs exhibit a pronounced cubo-octahedral geometry, the numerically simulated ND is approximated with a more symmetrical ellipsoidal geometry, whose semiaxes are extracted from an atomic force microscope (AFM) scan with $(r_x, r_y, r_z) = (40, 50, 22.5)$ nm; see Fig. 2(a). The SM provides details on the NDs synthesis and AFM measurements. Slightly immersing the ND along z into the substrate with a penetration depth $d = \xi r_z$ creates a contact area, where phonons can be exchanged with the bulk reservoir introducing a coupling rate. Figure 2(b) shows the simulated spectral density of states (DOS) $\rho(\nu)$ for the ND coupled to bulk with $\xi = 10^{-2}$, which reveals a quasilocalized ND mode around 75 GHz. Moreover, a polynomial fit [red dashed line in Fig. 2(b)] shows that the DOS approximately scales with $\rho(\nu) \propto \nu^{1.91}$ rather than quadratically, which is to be expected for a pure bulklike system, indicative of contributions from bound surface modes [9,17]. Using the strain susceptibilities $\alpha/2\pi = 1.3$ PHz/strain, $\beta/2\pi = -1.7$ PHz/strain in Eqs. (2) and (3) and the simulated coupled systems strain fields $\epsilon_{ij,n}(\vec{r})$, where the SiV^- high-symmetry axis is assumed along z, Eq. (4) is evaluated at each position in the xz plane [5]. Figure 2(c) shows the orbital lifetime ratio $T_1^0/T_1^{0,B}$, where $T_1^{0,B} \approx 209$ ns is obtained by averaging T_1^0 over the bulk, in good agreement with the analytical $T_1^{0,B} \approx 233$ ns. Note that Fig. 2(c) only shows a close-up of the ND in the xz plane. See SM for details on DOS evaluation, various material parameters, and geometries. This configuration reaches a maximum of $T_{1,\mathrm{max}}^0/T_1^{0,B} \approx 120$ at the center of the ND. As a rough estimate, $T_{1,\mathrm{max}}^0$ would extend the orbital lifetime at cryogenic temperatures of $T = 5$ K to $T_{1,\mathrm{max}} = T_{1,\mathrm{max}}^0 \coth(\hbar\Delta_{\mathrm{GS}}/2k_BT) \approx 5$ μs.

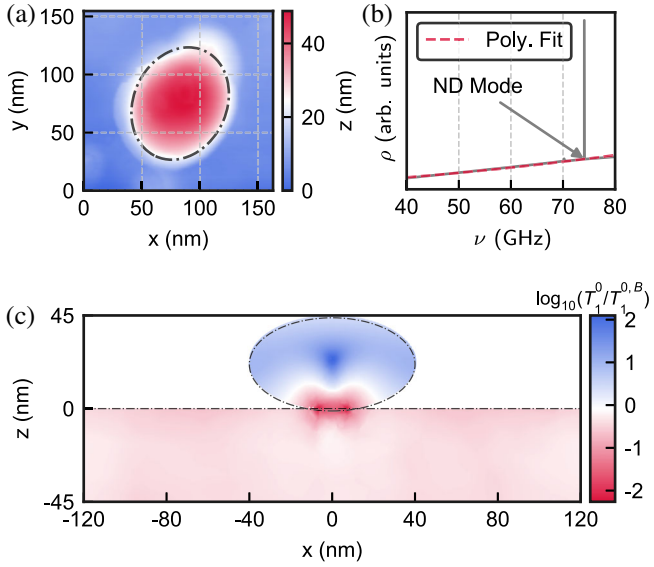

FIG. 2. (a) AFM scan of a ND revealing characteristic sizes of $(r_x, r_y, r_z) = (40, 50, 22.5)$ nm, setting an upper size limit for all consecutively measured ND samples. (b) Density of states (DOS) ρ as a function of frequency ν for the ND coupled to bulk with a penetration depth of $d = 0.01 r_z$. A polynomial fit shows a scaling of $\rho \propto \nu^{1.91}$ for the composite system. (c) FEM simulation of the relative local increase in orbital relaxation times compared to bulk, $T_1^0/T_1^{0,B}$.

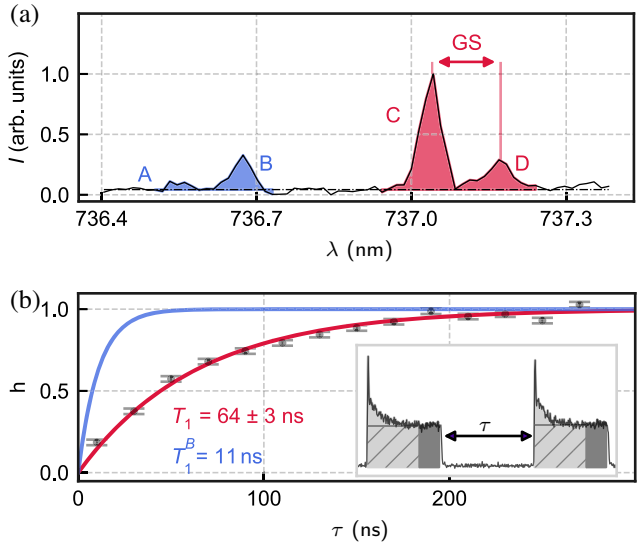

FIG. 3. (a) Photoluminescence intensity I as a function wavelength λ revealing the four-line structure of a SiV^- in a ND with a GS splitting of 72 GHz. (b) Peak heights h, determined from the fluorescence of a resonant pulse sequence, as a function of interpulse delay τ. The solid red and blue lines show a numerical fit to measurements and theory calculations, respectively. The inset illustrates the extraction of peak heights with extrapolation of stationary count rates (horizontal solid line) by the last 50 ns count trace (dark gray area).

Measurements.—T_1 is measured for 15 SiV^- in different NDs at local temperatures ranging from 4.6 up to 9.5 K. Single-emitter characteristics such as autocorrelation measurements on this sample have been performed in Ref. [18]. The NDs are coated onto a diamond substrate, selected for high thermal conductivity. The average height of 26 nm and lateral extension of 82 nm for the differently shaped NDs is determined with an AFM; see SM for details. The local temperature is evaluated by

$$\frac{N_{\mathrm{C+D}}}{N_{\mathrm{A+B}}} = \exp\left(-\frac{\hbar\Delta_{\mathrm{ES}}}{k_B T}\right), \tag{5}$$

where a Boltzmann distribution for the summed counts N in A,B and C,D is assumed, reflecting relative populations. The excited state (ES) splitting is determined from the spectrum of an off-resonantly excited SiV^-. Figure 3(a) shows an example ND spectrum.

T_1 is measured with a tailored pulse sequence resonant with transition C and consisting of several 200-ns-long pulses with an increasing interpulse delay τ [18]. The peak heights h are extracted by summing up all counts within each pulse and subtracting the stationary ones; see Fig. 3(b). h is then fitted with

$$h(\tau) \propto 1 - \exp\left(-\frac{\tau}{T_1}\right), \tag{6}$$

revealing a T_1 of (64 ± 3) for the SiV^- measured in Fig. 3(b).

To compare our measured values for T_1 at different T and $\Delta_{\mathrm{GS}}/2\pi$ to the corresponding maximally achievable bulk time T_1^B, which is solely limited by electron-phonon relaxation, an analytical expression,

$$(T_1^B)^{-1} = \frac{h[\alpha^2 + (\beta/2)^2]}{\pi\rho}\left(\frac{1}{5v_t^5} + \frac{2}{15v_l^5}\right)\Delta_{\mathrm{GS}}^3 \coth\left(\frac{\hbar\Delta_{\mathrm{GS}}}{2k_B T}\right), \tag{7}$$

with

$$v_t = \sqrt{\frac{E}{\rho}\frac{1}{2(1+\nu)}}, \qquad v_l = \sqrt{\frac{E}{\rho}\frac{1-\nu}{(1+\nu)(1-2\nu)}},$$

is used, where $E = 1050$ GPa and $\nu = 0.2$; see Fig. 4(a), dark gray line. The upper gray limit represents a bulk limit for $E = 1143$ GPa, $\nu = 0.0691$ at $T = 3.6$ K [19]. Equation (7) can be derived from Eq. (4) using a long-wavelength approximation [17,20].

The procedure is repeated for all other 14 NDs and the ratio T_1/T_1^B is depicted in Fig. 4(a) as a function of GS splitting. The color of each dot shows the temperature of the respective SiV^-. See SM for absolute timescales. For a GS splitting of 132 GHz a prolongation of the orbital lifetime of up to 8 can be observed. The triangle, diamond, and squared markers in Fig. 4(a) represent measured T_1 in a bulk diamond and diamond nanobeam, respectively, which were conducted under similar experimental conditions [6,7,9]. The above calculated T_1^B is a conservative estimation of the upper limit reachable in bulk diamond in the presence of resonant, single-phonon-dominated orbital relaxation. To our knowledge, experimentally measured T_1 in the low-strain regime stay below or within the theoretical limits [6,21].

Temperature-dependent measurements for the ND highlighted with a red star at $\Delta/2\pi \approx 87$ GHz indicate a single-phonon orbital relaxation with Γ_1 increasing linearly with T shown by the red regression line with a slope of 7 ± 1 MHz K^{-1} in Fig. 4(b). In comparison, for the correspondingly calculated bulk rates, a slope of 15 ± 1 MHz K^{-1} is determined, represented by the gray line.

In the temperature regime presented here, the orbital relaxation dominantly impairs the electron spin coherence by causing an additional random phase through recurring orbital excitation and relaxation while preserving the spin projection [22]. The resulting coherence is investigated for the ND highlighted with a red plus in Fig. 4(a) which exhibits a $T_1 = 46 \pm 5$ ns. The sample is placed inside a permanent magnet to split the orbital-degenerate spin states and make them optically accessible. Because of misalignment of the magnetic field with the defect's symmetry axis

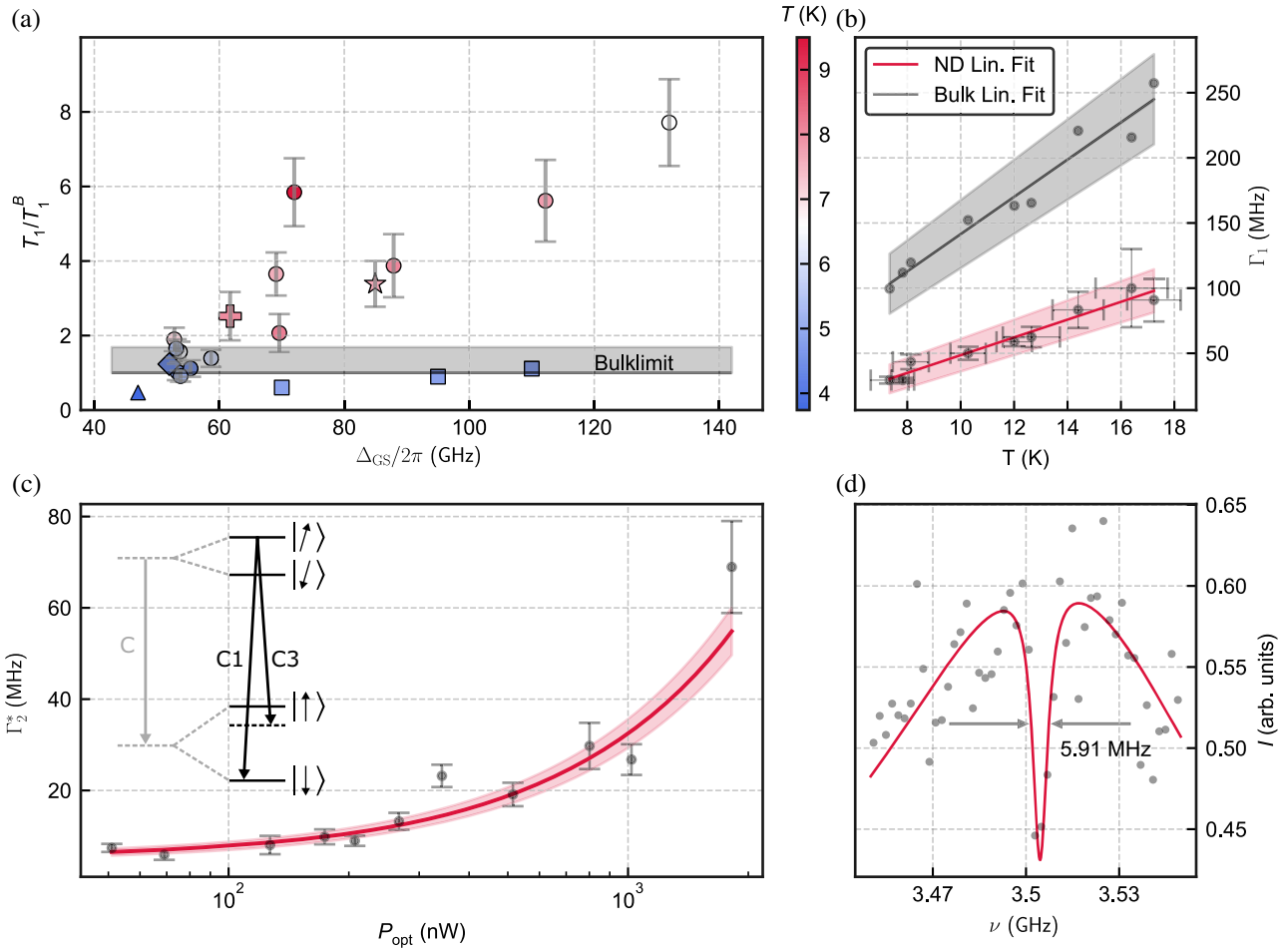

FIG. 4. (a) Orbital lifetime extension through comparison of measured T_1 and analytical bulk limit T_1^B for different GS splitting Δ_{GS} and temperatures T. The triangle and diamond marker represent measured T_1 in bulk from Refs. [6,7]. Moreover, the squared data points are measurements done inside a diamond nanobeam [9]. Bulk limits correspond to calculations with $E = 1050$ GPa, $\nu = 0.2$ (dark gray line) and $E = 1143$ GPa, $\nu = 0.0691$. (b) Temperature-dependent relaxation rate Γ_1 at $\Delta_{GS}/2\pi \approx 87$ GHz for the ND highlighted with a red star in (a) and corresponding bulk rates calculated with Eq. (7) with linear regression and standard deviation. (c) The spin states of the ND indicated by a red plus in (a) are linked in a Λ-type system of transition C1 and C3, as schematically illustrated. The total optical power P_{opt} of both fields is varied and the dark state's full width at half maximum Γ_2^* is extracted from a double-Lorentzian fit. The red line represents a linear regression with one standard-deviation fit error. (d) An example measurement of (c) with $\Gamma_2^* = 5.91 \pm 110$ MHz where the red line is illustrating a fit to the measured counts when sweeping the modulation frequency ν across C3 while continuously pumping C1.

and consequential spin mixing, spin-flipping transitions become optically allowed; see SM for details. Simultaneously driving transitions C1 and C3 with a resonant laser and the sideband of an electro-optical modulator forms a Λ-type system with the two ground-state and an additional excited-state spin; see the schematic level structure in Fig. 4(c). Tuning the modulation frequency ν to fulfill the Raman condition creates a coherent dark state. Varying ν reveals a Lorentzian dip with its minimum at Raman resonance, as shown in Fig. 4(d). The dark state's linewidth Γ_2^* is extracted from the full width at half maximum of a double-Lorentzian fit. From Γ_2^* the dephasing time T_2^* can be calculated by using the half width at half maximum $T_2^* = 1/(\pi\Gamma_2^*)$. Since the transition dipoles are broadened through the laser fields which ultimately broadens the dark state's linewidth, the coherent-population trapping (CPT) measurement is repeated for various optical powers P_{opt} and extrapolated to $P_{opt} = 0$ by fitting a linear regression. The extracted $\Gamma_2^* = 5.13 \pm 13$ MHz results in a dephasing time of $T_2^* = 62.1 \pm 3$ ns.

Discussion.—The results in Fig. 4(a) suggest an inverse correlation between T_1/T_1^B and ND size. On the one hand, reducing the size shifts the NDs mechanical eigenfrequencies to higher energies [20], which also enhances the respective mode's strain field [7,11]. As a result, a SiV^- can couple to these fields, which increases its GS splitting.

Consequential, thermally excited phonons from the surrounding ND or bulk are exponentially less likely populated, thus reducing Γ_1. On the other hand, smaller SiV^- host geometries exhibit reduced contact areas between ND and substrate which then suppresses the coupling to the bulk phonon bath, hence also reducing Γ_1. See SM for further simulations with a different geometry, contact areas, and ground-state splittings. Geometrical decoupling becomes apparent when looking at NDs with $\Delta_{GS}/2\pi \approx 70$ GHz in Fig. 4(a). The similar GS splittings indicate comparable ND geometries. However, the ND with a maximal temperature of $T = 9.5$ K exhibits the largest orbital lifetime ratio of $T_1/T_1^B \approx 6$. This might reveal a preferential orientation of the ND, whose contact area with the substrate is smallest and thus also isolated best. As a result, the phonon exchange with the substrate is reduced, which reduces Γ_1 and increases temperature.

The discrepancy between simulated orbital lifetime ratios and the ones which are determined from measurements is attributed to an unfavorable interplay of different mechanisms, leading to nontrivial coupling rates to the bulk. These broaden the ND resonances and bring their local phononic spectral densities closer to the one of bulk which limit the maximally achievable T_1/T_1^B. Firstly, although the NDs sizes are measured to be smaller than the simulated one, a contact area largely exceeding the one used in the simulations strongly enhances phonon exchange with the bulk. Secondly, the mechanical impedances of the ND and the diamond base substrate are similar, allowing for a high phonon transmission, which also increases coupling to the substrate.

Further validation of a modified phonon density of states can be concluded from the different temperature dependencies in Γ_1 inside the ND and bulk, respectively, which is proportional to the phonon spectral density; see Eq. (7).

In addition, the extrapolated dephasing time exceeds the theoretical phononically limited $T_2^{*,B} = 2T_1^B \approx 36$ ns for bulk diamond by roughly a factor of 2 at the NDs respective $\Delta_{GS}/2\pi \approx 62$ GHz and $T \approx 8$ K [22]. However, the CPT shows that T_2^* is not reaching its phononic limit at $2T_1 \approx 92$ ns. The mismatch can be attributed to several factors. First, local fluctuations of laser driving strength and spectral diffusion over the course of several minutes during the measurement alter the additional energy splitting from ac-Stark shifts thereby translating onto a shift of the Raman condition, which effectively broadens the line width. Second, loss of spin coherence due to surface effects or impurities.

Outlook.—The experimental results presented in this work show that the SiV^- orbital lifetime is extended up to a factor of 8 when incorporated into a small, tailored diamond host as compared to a SiV^- in bulk diamond. Consequently, the spin dephasing time is prolonged as validated by measuring the power-dependent Raman-resonance line width in CPT. In order to suppress the orbital relaxation further, nanomanipulation techniques utilizing an AFM can be used to rotate the NDs, thereby decreasing the contact area which leads to a more optimal isolation [18,23]. Moreover, using an engineered substrate material, e.g., a phononic crystal, to suppress phonons in the relevant spectral range reduces the impedance matching between the former and the ND, which yields a better isolated host [16].

Extending T_1 to the predicted 5 μs opens up the possibility to coherently control the SiV^- spin without relying on a dilution refrigerator. Decoupling from thermal phonons was shown for temperatures below 500 mK [1], where T_2^* is no longer limited by single-phonon processes.

Major impact arises from the NDs integration capabilities into integrated photonics and broadband antenna structures, where photonic and phononic properties can be merged to achieve coherent spin-photon control [24,25].

The project was funded by the Deutsche Forschungsgemeinschaft (DFG, German Research Foun dation) in Project No. 398628099, the Baden-Württemberg Stiftung in project Internationale Spitzenforschung, and IQst. M. W. D. acknowledges support from the Australian Research Council (DE170100169). Experiments performed for this work were operated using the Qudi software suite [26].

*These authors contributed equally to this work.
†Corresponding author.
alexander.kubanek@uni-ulm.de

[1] D. D. Sukachev, A. Sipahigil, C. T. Nguyen, M. K. Bhaskar, R. E. Evans, F. Jelezko, and M. D. Lukin, Silicon-Vacancy Spin Qubit in Diamond: A Quantum Memory Exceeding 10 ms with Single-Shot State Readout, Phys. Rev. Lett. **119**, 223602 (2017).

[2] M. K. Bhaskar, R. Riedinger, B. Machielse, D. S. Levonian, C. T. Nguyen, E. N. Knall, H. Park, D. Englund, M. Lončar, D. D. Sukachev, and M. D. Lukin, Experimental demonstration of memory-enhanced quantum communication, Nature (London) **580**, 60 (2020).

[3] J. L. Zhang, S. Sun, M. J. Burek, C. Dory, Y.-K. Tzeng, K. A. Fischer, Y. Kelaita, K. G. Lagoudakis, M. Radulaski, Z.-X. Shen, N. A. Melosh, S. Chu, M. Lončar, and J. Vučković, Strongly cavity-enhanced spontaneous emission from silicon-vacancy centers in diamond, Nano Lett. **18**, 1360 (2018).

[4] J. Lang, S. Häußler, J. Fuhrmann, R. Waltrich, S. Laddha, J. Scharpf, A. Kubanek, B. Naydenov, and F. Jelezko, Long optical coherence times of shallow-implanted, negatively charged silicon vacancy centers in diamond, Appl. Phys. Lett. **116**, 064001 (2020).

[5] S. Meesala, Y.-I. Sohn, B. Pingault, L. Shao, H. A. Atikian, J. Holzgrafe, M. Gündoğan, C. Stavrakas, A. Sipahigil, C. Chia, R. Evans, M. J. Burek, M. Zhang, L. Wu, J. L. Pacheco, J. Abraham, E. Bielejec, M. D. Lukin, M. Atatüre, and M. Lončar, Strain engineering of the silicon-vacancy center in diamond, Phys. Rev. B **97**, 205444 (2018).

[6] B. Pingault, D.-D. Jarausch, C. Hepp, L. Klintberg, J. N. Becker, M. Markham, C. Becher, and M. Atatüre, Coherent control of the silicon-vacancy spin in diamond, Nat. Commun. **8**, 15579 (2017).

[7] K. D. Jahnke, A. Sipahigil, J. M. Binder, M. W. Doherty, M. Metsch, L. J. Rogers, N. B. Manson, M. D. Lukin, and F. Jelezko, Electron–phonon processes of the silicon-vacancy centre in diamond, New J. Phys. **17**, 043011 (2015).

[8] M. H. Metsch, K. Senkalla, B. Tratzmiller, J. Scheuer, M. Kern, J. Achard, A. Tallaire, M. B. Plenio, P. Siyushev, and F. Jelezko, Initialization and Readout of Nuclear Spins via a Negatively Charged Silicon-Vacancy Center in Diamond, Phys. Rev. Lett. **122**, 190503 (2019).

[9] Y.-I. Sohn, S. Meesala, B. Pingault, H. A. Atikian, J. Holzgrafe, M. Gündoğan, C. Stavrakas, M. J. Stanley, A. Sipahigil, J. Choi, M. Zhang, J. L. Pacheco, J. Abraham, E. Bielejec, M. D. Lukin, M. Atatüre, and M. Lončar, Controlling the coherence of a diamond spin qubit through its strain environment, Nat. Commun. **9**, 2012 (2018).

[10] C. Hepp, T. Müller, V. Waselowski, J. N. Becker, B. Pingault, H. Sternschulte, D. Steinmüller-Nethl, A. Gali, J. R. Maze, M. Atatüre, and C. Becher, Electronic Structure of the Silicon Vacancy Color Center in Diamond, Phys. Rev. Lett. **112**, 036405 (2014).

[11] M.-A. Lemonde, S. Meesala, A. Sipahigil, M. J. A. Schuetz, M. D. Lukin, M. Loncar, and P. Rabl, Phonon Networks with Silicon-Vacancy Centers in Diamond Waveguides, Phys. Rev. Lett. **120**, 213603 (2018).

[12] See Supplemental Material at http://link.aps.org/supplemental/10.1103/PhysRevLett.128.153602 for additional details about the model as well as ND synthesis and characterization, which includes Refs. [13–15].

[13] A. N. Cleland, *Foundations of Nanomechanics: From Solid-State Theory to Device Applications* (Springer, Berlin, 2003).

[14] W. M. Lai, D. Rubin, and E. Krempl, *Introduction to Continuum Mechanics*, 4th ed. (Butterworth-Heinemann/Elsevier, Amsterdam, 2010).

[15] A. Norambuena, S. A. Reyes, J. Mejía-Lopéz, A. Gali, and J. R. Maze, Microscopic modeling of the effect of phonons on the optical properties of solid-state emitters, Phys. Rev. B **94**, 134305 (2016).

[16] I. Lekavicius, T. Oo, and H. Wang, Diamond Lamb wave spin-mechanical resonators with optically coherent nitrogen vacancy centers, J. Appl. Phys. **126**, 214301 (2019).

[17] K. V. Kepesidis, M.-A. Lemonde, A. Norambuena, J. R. Maze, and P. Rabl, Cooling phonons with phonons: Acoustic reservoir engineering with silicon-vacancy centers in diamond, Phys. Rev. B **94**, 214115 (2016).

[18] S. Häußler, L. Hartung, K. G. Fehler, L. Antoniuk, L. F. Kulikova, V. A. Davydov, V. N. Agafonov, F. Jelezko, and A. Kubanek, Preparing single SiV^{-1} center in nanodiamonds for external, optical coupling with access to all degrees of freedom, New J. Phys. **21**, 103047 (2019).

[19] C. A. Klein and G. F. Cardinale, Young's modulus and Poisson's ratio of CVD diamond, Diam. Relat. Mater. **2**, 918 (1993).

[20] A. Albrecht, A. Retzker, F. Jelezko, and M. B. Plenio, Coupling of nitrogen vacancy centres in nanodiamonds by means of phonons, New J. Phys. **15**, 083014 (2013).

[21] L. J. Rogers, K. D. Jahnke, M. H. Metsch, A. Sipahigil, J. M. Binder, T. Teraji, H. Sumiya, J. Isoya, M. D. Lukin, P. Hemmer, and F. Jelezko, All-Optical Initialization, Readout, and Coherent Preparation of Single Silicon-Vacancy Spins in Diamond, Phys. Rev. Lett. **113**, 263602 (2014).

[22] J. N. Becker, B. Pingault, D. Groß, M. Gündoğan, N. Kukharchyk, M. Markham, A. Edmonds, M. Atatüre, P. Bushev, and C. Becher, All-Optical Control of the Silicon-Vacancy Spin in Diamond at Millikelvin Temperatures, Phys. Rev. Lett. **120**, 053603 (2018).

[23] L. J. Rogers, O. Wang, Y. Liu, L. Antoniuk, C. Osterkamp, V. A. Davydov, V. N. Agafonov, A. B. Filipovski, F. Jelezko, and A. Kubanek, Single $Si - V^{-}$ Centers in Low-Strain Nanodiamonds with Bulklike Spectral Properties and Nanomanipulation Capabilities, Phys. Rev. Applied **11**, 024073 (2019).

[24] K. G. Fehler, A. P. Ovvyan, L. Antoniuk, N. Lettner, N. Gruhler, V. A. Davydov, V. N. Agafonov, W. H. Pernice, and A. Kubanek, Purcell-enhanced emission from individual SiV^{-1} center in nanodiamonds coupled to a Si_3N_4-based, photonic crystal cavity, Nanophotonics **9**, 3655 (2020).

[25] R. Waltrich, B. Lubotzky, H. Abudayyeh, E. S. Steiger, K. G. Fehler, N. Lettner, V. A. Davydov, V. N. Agafonov, R. Rapaport, and A. Kubanek, High-purity single photons obtained with moderate-NA optics from SiV center in nanodiamonds on a bullseye antenna, New J. Phys. **23**, 113022 (2021).

[26] J. M. Binder, A. Stark, N. Tomek, J. Scheuer, F. Frank, K. D. Jahnke, C. Müller, S. Schmitt, M. H. Metsch, T. Unden, T. Gehring, A. Huck, U. L. Andersen, L. J. Rogers, and F. Jelezko, Qudi: A modular python suite for experiment control and data processing, SoftwareX **6**, 85 (2017).